Influence of the Statistical Properties of Phase and Intensity on Closure Phase

Yusuf Eshqi Molan⬤, Zhong Lu⬤, and Jin-Woo Kim⬤

Abstract—**Nonzero closure phase exists in multilooked pixels. We study the influence of the statistical properties of the intensity and phase changes of single-looked pixels on multilooked phase and coherence. By quantifying the extent of their influences on phase triplet, we show in this article that the statistical properties of the intensity of pixels within a multilooking window can induce changes in interferometric phase and coherence, and contribute to the nonzero closure phase. We demonstrate that the intensity-induced changes increase by increasing the standard deviation of the phase changes, dispersion index of intensity, and the correlation between the intensity and phase changes. We have used ALOS Phased Array type L-band Synthetic Aperture Radar (PALSAR), ALOS-2 PALSAR-2, and Sentinel-1 images to generate real and semisynthetic interferograms to assess our findings. The semisynthetic interferograms are produced by pairing real SAR data and synthetic SAR data; the synthetic SAR data are generated from the real data by adding random vectors with predefined average changes of phase and intensity. Our results show that closure phase is only a function of the statistical properties of the phase and intensity of pixels, and does not possess the information about the magnitude of physical changes. This casts doubt on the effectiveness of methods that exploit phase triplet as a means to estimate soil moisture or any other deforming or nondeforming changes.**

Index Terms—**Closure phase, coherence, interferometric phase, single-looked pixel's intensity and phase changes.**

I. INTRODUCTION

INTERFEROMETRIC synthetic aperture radar (InSAR) has the ability to remotely sense millimeter to centimeter scale surface deformation with a high spatial resolution of tens of meters or better, irrespective of weather and time of day [1], [2]. Surface deformations due to various mechanisms, such as volcanism, subsidence, permafrost, and landslides, have been successfully detected using InSAR [3]–[9]. In addition to deformation mapping, interferometric phase has been also used to estimate soil moisture changes [10]–[12]. The common approach in the literature to estimate soil moisture is to define a relationship between the mean soil moisture value and InSAR phase and intensity changes. This is because the change in soil moisture will induce a change in

dielectric constant. Dielectric constant of soil manipulates the depth and the attenuation of electromagnetic waves penetrating the soil. Basically, the depth of penetration decreases but at the same time wavenumber increases by increasing soil moisture. This leads to phase increase, which is manifested as subsidence on interferograms [12], [14].

The phase of interferograms generated from single-looked pixels are rather noisy because of the strong effects of decorrelations and noises. One way to deal with this problem is using multilooked interferograms. Multilooking reduces the noise and improves the reliability of phase unwrapping by averaging adjacent pixels in the complex interferogram [15], [16]. Another approach is by exploring SqueeSAR [15], and the component extraction and selection SAR (CAESAR) algorithms [17], [18], which have been developed to extend Persistent Scatterers Interferometry (PSI) analysis. SqueeSAR overcomes the influence of temporal and geometrical decorrelation on Distributed Scatterers (DSs) in nonurban areas [15], [17], [18]. The strength of CAESAR is the possibility of extracting multiple dominant scattering mechanisms within a resolution element based on the analysis of the covariance matrix [18].

Multilooking, however, leads to nonzero phase triplet. Two SAR images from the same orbital track taken at different times can be used to generate a multilooked interferogram. Likewise, using three SAR images, three mutual interferograms can be generated. One may assume that the phase of the multilooked interferogram pairing the first and the last SAR images equals the summation of the phases of the two intermediate interferograms. In the real world, however, the assumption is violated because experiences show otherwise; this phenomenon is known as phase inconsistency.

The possible causes of nonzero phase triplet have been recently discussed in the literature. Zan *et al.* [10] argued that phase inconsistencies can arise when different scatterer populations with independent phase behaviors interfere with each other. They illustrated that changes in the water content of soil and vegetation could contribute to phase inconsistency. The 3-D structure of the scatterers within the resolution cell can also possibly cause phase inconsistency in the case of a nonzero spatial baseline [10]. Zwieback *et al.* [11] argued that apart from deformations, which do not cause phase inconsistency, there should be other factors influencing phase inconsistency. The authors attributed the phase inconsistencies to nonrandom effects of decorrelation noise, the change in dielectric constant, and nonzero spatial baselines. The phase inconsistency induced by the changes in dielectric constant has been reported in the observations and interferometric models

introduced recently [10]. The change in dielectric constant is ascribed to the change in soil moisture and water content of vegetation [10]–[12] and also to the freeze-thaw condition of soil [11].

Unlike the previous studies that attribute nonzero phase closure to the changes in 3-D-structure or dielectric constant of single-looked pixels, in this article, we show that nonzero phase triplet is only related to the statistical properties of the pixels within the multilooked window. One simple reason for this argument is that phase inconsistency, that is nonzero phase triplet, does not exist in single-looked images but rather only in multilooked images. Therefore, analyzing the influence of the statistical properties of intensity and phase changes of single-looked pixels on multilooked phase would quantify the extent of their influence on phase triplet.

Multilooked phase and coherence are the functions of phase (deforming and nondeforming) changes of single-looked pixels and the way that the physical changes are distributed in the multilooking window [19]–[21]. This is to say that the multilooked phase contains a physical phase and a statistical phase. Therefore, we first quantify the contributions of physical changes and the statistical properties of pixels on multilooked phase and coherence, and then assess the extent of their influences on closure triplet. Specifically, we answer the question: does the nonzero phase triplet demonstrates the statistical characteristics of multilooked window or does it instead possess information about phase changes corresponding to absolute physical changes, that is deforming and nondeforming processes such as soil moisture changes. This is of great importance because if the former statement is true, closure phase cannot be used as a proxy for estimating the physical changes in the pixels.

This article is structured as follows: Section II analyzes multilooked phase, coherence, and closure phase; Section III includes the multilooked interferometric phase generated from synthetic data, and presents the results of interferometric phase and coherence along with phase triplet. Section IV provides results generated using real SAR data and a discussion of the results; and finally, conclusions appear in Section V.

II. METHODS

A. Multilooked Interferometric Phase

Let $u_1 = [u_1^1, u_1^2, \ldots, u_1^n]'$ and $u_2 = [u_2^1, u_2^2, \ldots, u_2^n]'$ to be master and slave SAR images each containing n pixels. Every pixel on each image is a random speckled quantity, and can be written as the product of the unspeckled physical quantity s_i^k and the independent speckle random process n_i^k [19]–[21]

$$u_i^k = s_i^k \cdot n_i^k \tag{1}$$

where k is the pixel position. It is noted that throughout the article, superscripted parenthesized numbers indicate the pixel numbers, subscripted numbers show the image numbers, and subscripted letters indicate the association. In addition, bold letters represent the vectors.

The noise vector is a zero-mean value complex Gaussian random vector with the phase that is uniformly distributed over $[-\pi, \pi]$ [21]–[25]. For the two images, n_1 and n_2

are statistically independent of each other and of s_1 and s_2 [19]. Therefore, u_1 and u_2 are zero-mean random complex variables. Hence, the coherence of two complex SAR images u_1 and u_2 is defined as follows [21]–[23]:

$$\gamma = \frac{E\left[u_1 u_2^*\right]}{\sqrt{E[|u_1|^2]E[|u_2|^2]}} = |\gamma|e^{i\varphi_0} \tag{2}$$

where φ_0 is the expected noise-free phase, u_2^* is the complex conjugate of the second image, and $E[.]$ denotes the expectation value that in practice will be approximated with a sampled average [19]–[21]. Hence, over statistically uniform areas, the sampled coherence can be computed as [22]–[25]

$$\hat{\gamma} = \frac{\sum_1^n u_1 u_2^*}{\sqrt{\sum_1^n |u_1|^2 \sum_1^n |u_2|^2}} = |\hat{\gamma}|e^{j(\varphi_0 + \varphi_n)} = |\hat{\gamma}|e^{i\varphi} \tag{3}$$

where $|\hat{\gamma}|$ and φ are the magnitude and phase of the multilooked interferogram. The joint probability density function (PDF) of magnitude and phase of an interferogram depends on the number of looks and satisfies the Wishart distribution. The marginal PDF of InSAR phase can be derived from the joint PDF [19], [24]–[28] that is characterized with a mean of φ_0 and a variance, which is a function of InSAR coherence value $|\gamma|$ [27], [28]. Thus, we have

$$\varphi = \varphi_0 + \varphi_n \text{ with } E[\varphi] = \varphi_0 \tag{4}$$

where φ_n denotes a zero-mean additive noise, upon which its variance is independent of the magnitude φ [27]. The expected value of interferometric phase is φ_0 regardless of the magnitude of changes, the number of looks, and the value of complex correlation coefficient [21]–[27].

B. Influence of Intensity and Phase Changes of Single-Looked Pixels on Multilooked Pixel's Phase

Some physical processes, that is deforming or nondeforming changes, can cause intensity changes as well as phase changes. Soil moisture and vegetation biomass changes, for instance, initiate dielectric constant changes that in turn cause intensity and phase changes [10], [11], [29], [30]. This is to say that in addition to phase changes of the pixels that occur between two images taken at different times, their intensities are also subject to change. Plus, the two variables may be correlated with some degree. Basically, the amplitude and the phase of SAR images are statistically independent random variables [22]–[28], [31]. However, between two images that are used to generate an interferogram, the intensity of pixels and their phase changes may not be independent variables. Therefore, we quantify the contribution of the statistical characteristics of intensity changes within the multilooking window, and the correlation between intensity and phase changes on the multilooked phase and coherence. By considering $u = ae^{j(\theta_1)}$ in (2), we can rewrite (2) as

$$\gamma = \frac{E\left[u_1 u_2^*\right]}{\sqrt{E[|u_1|^2]E[|u_2|^2]}} = \frac{E[I_{1,2}e^{j(\theta_{1,2})}]}{\sqrt{E[I_1]E[I_2]}}$$

$$= \frac{1}{\sqrt{E[I_1]E[I_2]}}(E[I_{1,2}]E[e^{j(\theta_{1,2})}] + \text{cov}(I_{1,2}, e^{j(\theta_{1,2})}))$$

$$= |\gamma_0|e^{j(\varphi_0)} + |\gamma_s|e^{j(\varphi_s)}. \tag{5}$$

This article has been accepted for inclusion in a future issue of this journal. Content is final as presented, with the exception of pagination.

ESHQI MOLAN *et al.*: INFLUENCE OF THE STATISTICAL PROPERTIES OF PHASE AND INTENSITY 3

In the equations above $I_{1,2} = a_1 \cdot a_2$ is the vector of the product of the amplitudes of the first and second images, and $\theta_{1,2} = \theta_1 - \theta_2$ is the vector of their phase differences. The coherence vector γ is the vector summation of two vectors. The amplitudes of the vectors are $|\gamma_0|$ and $|\gamma_s|$, and their phases are φ_0 and φ_s. The angle of coherence can be written in terms of the expected phase φ_0

$$\arg\{\gamma\} = \varphi_0 + \Delta\varphi_{\text{cov}} \tag{6}$$

where $\Delta\varphi_{\text{cov}}$ is the phase change due to the influence of $\text{cov}(I_{1,2}, e^{j(\theta_{1,2})})$ and can be calculated using (5)

$$\Delta\varphi_{\text{cov}} = \arg\{E[I_{1,2}e^{j(\theta_{1,2})}]\} - \arg\{E[e^{j(\theta_{1,2})}]\}. \tag{7}$$

Similarly, the sampled coherence, that is interferogram, can be rewritten as

$$
\begin{aligned}
\hat{\gamma} &= \frac{1}{\frac{1}{n}\sqrt{\sum_{k=1}^{n} I_1^k \sum_{k=1}^{n} I_2^k}} \\
&\quad \times \left(\frac{1}{n^2} \left(\sum_{k=1}^{n} I_{1,2}^k \sum_{k=1}^{n} e^{j(\theta_{1,2}^k)} \right) + \text{cov}(I_{1,2}, e^{j(\theta_{1,2})}) \right) \\
&= |\hat{\gamma}_0| e^{j(\varphi_0')} + |\hat{\gamma}_s| e^{j(\varphi_s)}
\end{aligned} \tag{8}
$$

where $\varphi_0' = \varphi_0 + \varphi_{n,0}$. It is noted that that the superscripts indicate the pixel numbers and subscripts show the image numbers. The sampled coherence vector $\hat{\gamma}$ is the vector summation of two vectors with the angles of φ_0' and φ_s and the amplitudes of $|\hat{\gamma}_0|$ and $|\hat{\gamma}_s|$. φ_0' is dominated with the expected phase φ_0 plus a zero-mean random phase $\varphi_{n,0}$, which corresponds to the statistical properties of the phase changes within the multilooking window. φ_s is, however, associated with the statistical properties of the intensity and phase changes of the pixels. Similarly, the interferometric phase can be expressed as

$$
\begin{aligned}
\varphi &= \arg\{|\hat{\gamma}_0| e^{j(\varphi_0')} + |\hat{\gamma}_s| e^{j(\varphi_s)}\} = \varphi_0' + \Delta\varphi_{\text{cov}} \\
&= \varphi_0 + \varphi_n + \Delta\varphi_{\text{cov}}
\end{aligned} \tag{9}
$$

where $\Delta\varphi_{\text{cov}}$ is the phase change due to the influence of $\text{cov}(I_{1,2}, e^{j(\theta_{1,2})})$ on the interferogram's phase that can be calculated using (9)

$$\Delta\varphi_{\text{cov}} = \arg\left\{\sum_{k=1}^{n} I_{1,2} e^{j(\theta_{1,2}^k)}\right\} - \arg\left\{\sum_{k=1}^{n} e^{j(\theta_{1,2}^k)}\right\}. \tag{10}$$

In this article, φ_0' and $\Delta\varphi_{\text{cov}}$ are called intensity-independent and intensity-dependent phases, respectively, for simplicity. The intensity-independent phase represents the expected physical changes φ_0, for example deformation and soil moisture change, of single-looked pixels plus a zero-mean random phase φ_n, which is related to phase statistics within the multilooking window. In other words, the intensity-independent phase is related to the physical phase and the statistical properties of single-looked pixels' phase. The intensity-dependent phase, on the other hand, is associated with the statistical properties of both phase and intensity of single-looked pixels [see (5)–(7)].

C. Coherence Changes Related to the Statistical Properties of Single-Looked Pixels' Intensity and Phase

The coherence changes induced by $\text{cov}(I_{1,2}, e^{j(\theta_{1,2})})$ is calculated in (5) and (8). Considering the sampled coherence as

$$|\hat{\gamma}| = ||\hat{\gamma}_p| e^{j(\varphi_0')} + |\hat{\gamma}_s| e^{j(\varphi_s')}|. \tag{11}$$

We can calculate the coherence changes that is induced by the statistical properties of the phase and intensity of pixels

$$\Delta|\hat{\gamma}_{\text{cov}}| = ||\hat{\gamma}_p| e^{j(\varphi_0')} + |\hat{\gamma}_s| e^{j(\varphi_s')}| - ||\hat{\gamma}_p| e^{j(\varphi_0')}| \tag{12}$$

where $\Delta|\hat{\gamma}_{\text{cov}}|$ is the coherence change induced by $\text{cov}(I_{1,2}, e^{j(\theta_{1,2})})$ and is called intensity-dependent coherence in this article.

D. Contribution of Statistical Properties of Single-Looked Pixels' Intensity and Phase on Phase Closure

Three SAR images from the same orbital track taken at different times can be used to generate three multilooked interferograms. Closure phase is the difference between the phase of the interferogram pairing the first and the last SAR images and the summation of the phases of the two intermediate interferograms. For multilooked pixels with $\text{cov}(I_{1,2}, e^{j(\theta_{1,2})}) = 0$, using (4), we can write

$$\dddot{\varphi} = \varphi_{0,1} + \varphi_{n,1} + \varphi_{0,2} + \varphi_{n,2} - \varphi_{0,3} - \varphi_{n,3} \tag{13}$$

where $\dddot{\varphi}$ is the closure phase. By considering $\varphi_{0,1} + \varphi_{0,2} - \varphi_{0,3} = 0$, we have

$$\dddot{\varphi} = \varphi_{n,1} + \varphi_{n,2} - \varphi_{n,3} = \dddot{\varphi}_n. \tag{14}$$

It should be noted that the noise phases are zero-mean random variables that are related to the magnitude of the coherence, which is related to the standard deviation of phase changes of the pixels within the multilooking window. Thus, we have

$$E[\dddot{\varphi}] = 0 \text{ and } \sigma_\varphi = \sqrt{\sigma_{\varphi_{n_1}}^2 + \sigma_{\varphi_{n_2}}^2 + \sigma_{\varphi_{n_3}}^2}. \tag{15}$$

Likewise, the closure phase of a multilooked pixel with $\text{cov}(I_{1,2}, e^{j(\theta_{1,2})}) \neq 0$ can be stated as

$$\dddot{\varphi}' = \dddot{\varphi}_n + \Delta\dddot{\varphi}_{\text{cov}} \tag{16}$$

with the expected value and standard deviation of

$$E[\dddot{\varphi}] = \Delta\dddot{\varphi}_{\text{cov}} \text{ and } \sigma_{\dddot{\varphi}} = \sqrt{\sigma_{\sigma\cdot\dddot{\varphi}}^2 + \sigma_{\Delta\dddot{\varphi}_{\text{cov}}}^2} \tag{17}$$

where $\Delta\dddot{\varphi}_{\text{cov}} = \Delta\varphi_{\text{cov},1} + \Delta\varphi_{\text{cov},2} - \Delta\varphi_{\text{cov},3}$ is the contribution of intensity-dependent phase ($[\Delta\varphi_{\text{cov}}$ in (9)] of the three interferograms to the closure phase. Comparing (14) and (16), we can see that over pixels with $\text{cov}(I_{1,2}, e^{j(\theta_{1,2})}) = 0$, phase triplet is a function of phase distribution within the multilooked window, φ_n, with the expected value of zero. In other words, over pixels with intensity homogeneity, that is the intensity dispersion index $D_I = \sigma_{I_{1,2}}/\bar{I}_{1,2} = 0$, the expected value of closure phase is zero. Yet, for the cases where $\text{cov}(I_{1,2}, e^{j(\theta_{1,2})}) \neq 0$, it also contains contributions from the statistical properties of intensity as well as phase, $\Delta\varphi_{\text{cov}}'$.

III. SEMISYNTHETIC DATA

A. Semisynthetic Interferograms

The equations in Section II calculate the influence of the statistical properties of intensity and phase changes on interferometric phase and coherence and closure phase. Herein, we investigate their effect by exploiting semisynthetic interferograms. The first image of the semiinterferograms is a real SAR image and the second image is synthetic data generated from the real data by applying a predefined intensity and phase changes when compared with the first image. Imagine a patch on an SAR data containing $p \cdot q = n$ pixels, which is called image one $\mathbf{Z_1}$ here. Image two $\mathbf{Z_2}$ can be generated by adding a change to the vector $\mathbf{\Delta Z_{1,2}}$ to $\mathbf{Z_1}$ as

$$\mathbf{Z_2} = \mathbf{\Delta Z_{1,2}} + \mathbf{Z_1} \qquad (18)$$

where

$$\mathbf{\Delta Z_{1,2}} = \left[\Delta Z_{1,2}^{(1)}, \Delta Z_{1,2}^{(2)}, \ldots, \Delta Z_{1,2}^{(n)} \right]'. \qquad (19)$$

Each element of the change vector is associated with an intensity ratio $\alpha_{1,2}^{(i)} = I_2^{(i)}/I_1^{(i)}$, and a phase change $\Delta \theta_{1,2}^{(i)} = \theta_2^{(i)} - \theta_1^{(i)}$ so that for ith pixels of image one and two, we can write

$$Z_1^{(i)} = \sqrt{I_1^{(i)}} \exp\left(j\theta_1^{(i)}\right)$$
$$Z_2^{(i)} = \sqrt{\alpha_{1,2}^{(i)} I_1^{(i)}} \exp\left(j\left(\theta_1^{(i)} + \Delta\theta_{1,2}^{(i)}\right)\right). \qquad (20)$$

The intensity ratio and phase change vectors are random variables

$$\boldsymbol{\alpha} = \overline{\alpha} + \boldsymbol{n_\alpha} \text{ and}$$
$$\boldsymbol{\Delta\theta} = \overline{\Delta\theta} + \boldsymbol{n_{\Delta\theta}} \qquad (21)$$

where $\overline{\alpha}$ and $\overline{\Delta\theta}$ are the average intensity ratio and phase change, and $\boldsymbol{n_\alpha}$ and $\boldsymbol{n_{\Delta\theta}}$ are zero-mean random variable vectors. The intensity and phase of SAR images have exponential and uniform distributions, respectively, [25], [26], [31]. Therefore, by applying random vectors of intensity ratio and phase changes, the distribution properties of a real SAR image's intensity and phase will be preserved in the synthetic image $\mathbf{Z_2}$.

This allows to generate an interferogram between the two images that have predefined phase and intensity differences represented as random variable vectors. Fig. 1 shows a series of histograms of interferometric phases. Each of the histograms was generated from 200 000 semisynthetic interferograms. The first image of the semisynthetic interferograms is a patch of real SAR data including L-band ALOS Phased Array type L-band SAR (PALSAR), ALOS-2 PALSAR-2, and C-band Sentinel-1. The size of the patch for ALOS PALSAR and ALOS-2 PALSAR-2 images is 14 × 7 pixels in azimuth and range, respectively. For Sentinel-1 images, it is 20 × 4 pixels in azimuth and range, respectively. For each interferogram, the second image was generated by applying random intensity and phase changes to the pixels of the first image.

The first cluster of interferograms ('Cluster 1', blue histograms in Fig. 1) was generated by considering intensity
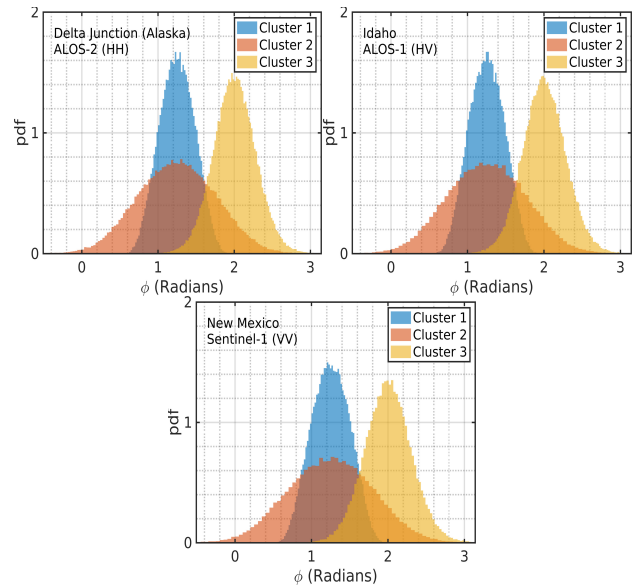

Fig. 1. PDF of interferometric phases over Delta Junction, Alaska (forest), Idaho (sparsely vegetated soil), and New Mexico (agricultural field). Cluster 1 has phase changes with no intensity changes. Cluster 2 has changes over non-homogeneous pixels where both intensity and phase changed. Like Cluster 2, Cluster 3 also has changes over nonhomogeneous pixels, but Cluster 3 has a correlation coefficient between intensity and phase change of 0.75 (versus 0.0 for Cluster 2).

homogeneity of the images. This means the amplitude of all pixels on every pair of images is considered to be one. Therefore, only the vector of phase changes was used. This cluster of interferograms represents phase changes over an ideal homogenous pixel (intensity homogeneity). The average and standard deviation of phase change are +1.25 and 1.0 rad, respectively. Fig. 1 (blue) illustrates the PDF of interferometric phases of cluster one. It should be noted that we used images from over a wide variety of land cover types with different multilooking numbers and different magnitudes of intensity and phase changes. However, we only show results from over three regions: Delta Junction, Alaska, Idaho, and New Mexico, where the multilooked pixel patches were selected over forest, sparsely vegetated soil, and agricultural fields, respectively. As shown in Fig. 1 and in general, the interferometric phase values φ center at φ_0 [see (2) and (4)] regardless of the wavelength and polarization of data, the magnitude of the changes, and the land cover type.

The second cluster of interferograms represents interferometric phase changes over a nonhomogeneous pixel where both intensity and phase changed. For this cluster, we used the same phase change vectors applied to generate the first cluster. The intensity of the second image was, however, generated by applying an average and standard deviation of changes of +4 and 3 dB to the intensity of the first image.

As discussed previously, some natural processes, such as soil moisture and vegetation biomass changes, may induce correlated phase and intensity changes. Next, we investigated the effect of correlated intensity and phase changes on interferometric phase and coherence. For doing this, the third cluster of interferograms was generated by applying the same changes in intensity and phase applied to generate the second cluster.

This article has been accepted for inclusion in a future issue of this journal. Content is final as presented, with the exception of pagination.

ESHQI MOLAN *et al.*: INFLUENCE OF THE STATISTICAL PROPERTIES OF PHASE AND INTENSITY 5

However, they differ in their correlation coefficients between intensity and phase changes, which are 0.0 and 0.75 for the second and third clusters, respectively. The third cluster of interferometric phase values centers at $\Delta\varphi_{\mathrm{cov}}$ [see (9) and (10)], which is the phase shift due to the influence of $\mathrm{cov}(\boldsymbol{I}_{1,2}, e^{j(\boldsymbol{\theta}_{1,2})})$ on the interferogram's phase. The coherence of the third cluster is also greater than the second one [see (11) and (12)].

Fig. 1 shows that for each cluster of interferograms, all three histograms over different land cover types center at the same angle. It can be seen that the coherence of interferograms, however, differs depending on the polarization combination, wavelength, land cover type, homogeneity of pixels, and the covariance between intensity and phase changes. It is noted that the height of a histogram is a measure of its coherence. In other words, coherent interferograms have thinner histograms due to noise reduction.

B. Closure Phase of Semisynthetic Interferograms

Synthetic data were also used to investigate the influence of the statistical properties of pixels on closure phase. For doing this, two categories of closure phases were generated, that is the closure phases of interferograms with independent intensity and phase changes (Cluster 2), and the closure phases of interferograms with correlated intensity and phase changes (Cluster 3). For each category, three types of closure phases were generated so that we have six types of closure phases in total, which are 2-a, 2-b, 2-c, 3-a. 3-b, and 3-c). For 2-a and 3-a types, the average phase changes of $+1.0$, $+0.5$, and -1.5 have been applied to generate three interferograms of a closure phase. For 2-b and 3-b types, half of the phase changes ($+0.5$, $+0.25$, and -0.75) is applied to generate three interferograms. For 2-c and 3-c types, zero phase changes were applied to generate the interferograms. Fig. 2 shows the histogram of closure phase for the second and third cluster of interferograms (see Fig. 1). It is noted that each interferogram histogram is generated from 200 000 semisynthetic interferograms.

It can be seen that the histogram of closure phase corresponding to the second cluster centers at zero, which is suggested by (15). For the third cluster, however, the histograms centers at $\Delta\ddot{\ddot{\varphi}}_{\mathrm{cov}}$ [see (17)]. It is noted that the results for the first cluster of interferograms (not shown here) are similar to the results of the second cluster.

IV. REAL DATA INTERFEROGRAMS AND DISCUSSION

A. Real Data Interferograms

Equation (9) shows that interferometric vector is a summation of two vectors, which are called intensity-independent and intensity-dependent components in this article. Examples of both the intensity-independent and intensity-dependent vectors are illustrated in Fig. 3. In Fig. 3, the interferometric vector and its first and second components are illustrated in green, blue, and red, respectively. The angle of the first vector φ'_0 is dominated by change in the physical properties of the pixels, expected phase φ_0, plus a zero-mean random phase $\varphi_{0,n}$, which corresponds to the statistical properties of the phase changes within the multilooking window. Therefore, its expected
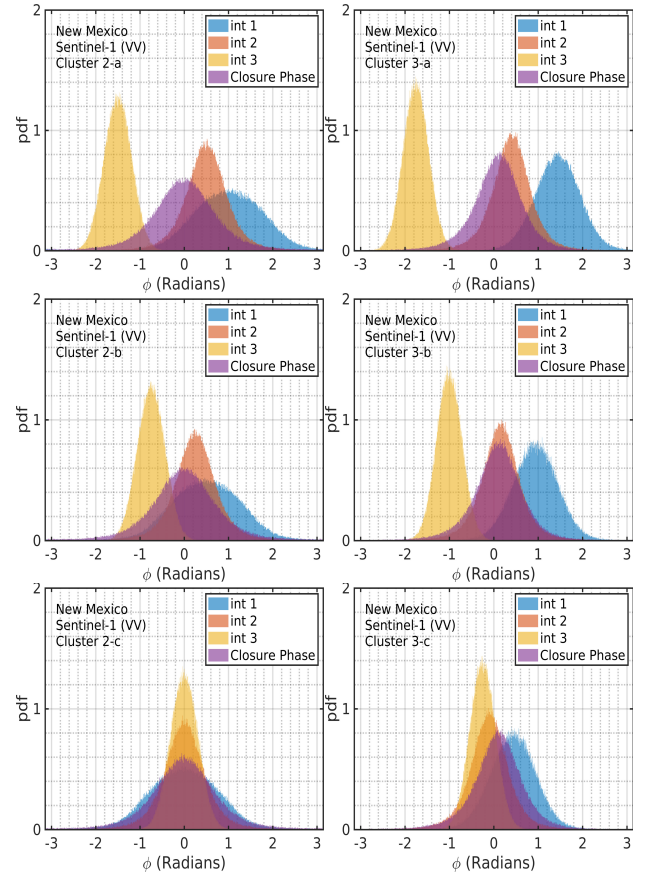

Fig. 2. PDF of closure phase over New Mexico (sparsely vegetated soil). In the legend, int 1, int 2, and int 3, respectively, represent the histograms of the first, second, and third interferograms.
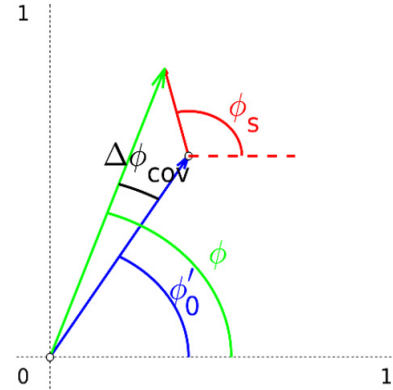

Fig. 3. Interferometric [φ in (9)], intensity-independent [φ'_0 in (9)], and intensity-dependent [$\Delta\varphi_{\mathrm{cov}}$ in (9)] vectors and phases. φ_s is the phase of $\mathrm{cor}(\boldsymbol{I}_{1,2}, e^{j(\boldsymbol{\theta}_{1,2})})$ [see (10)].

value is φ_0. The angle of the second vector φ_s, however, is associated with the statistical properties of the intensity and phase changes of the pixels. It is a function of the dispersion index of intensity $D_I = \sigma_{\boldsymbol{I}_{1,2}}/\bar{I}_{1,2}$, the standard deviation of the phase changes $\sigma_{e^{j(\boldsymbol{\theta}_{1,2})}}$, and the correlation coefficient between $\boldsymbol{I}_{1,2}$ and $e^{j(\boldsymbol{\theta}_{1,2})}$

$$\frac{\mathrm{cov}(\boldsymbol{I}_{1,2}, e^{j(\boldsymbol{\theta}_{1,2})})}{\frac{1}{n}\sqrt{\sum_{k=1}^{n} \boldsymbol{I}_1^k \sum_{k=1}^{n} \boldsymbol{I}_2^k}} = D_I \sigma_{e^{j(\boldsymbol{\theta}_{1,2})}} \mathrm{cor}(\boldsymbol{I}_{1,2}, e^{j(\boldsymbol{\theta}_{1,2})}). \quad (22)$$

This article has been accepted for inclusion in a future issue of this journal. Content is final as presented, with the exception of pagination.

6   IEEE TRANSACTIONS ON GEOSCIENCE AND REMOTE SENSING

Fig. 4. Study area in Delta Junction, Alaska (red box). The three major land cover types on the images are scarcely to moderately vegetated soil (area I), heavily vegetated area–forest (area II), and agricultural field (area III).

Its value is zero when either the dispersion index of intensity or the standard deviation of the phase changes is zero that is over pixels with intensity or phase homogeneities. Also, its value becomes zero when $\mathrm{cor}(\boldsymbol{I}_{1,2}, e^{j(\boldsymbol{\theta}_{1,2})}) = 0$.

Fig. 3 also shows an interferometric phase φ in green. It can be seen that the interferometric phase is a scalar summation of intensity-independent φ'_0 and intensity-dependent $\Delta\varphi_{\mathrm{cov}}$ phases. By comparing the two angles illustrated in Fig. 3, $\arg\{E[e^{j(\boldsymbol{\theta}_{1,2})}]\}$ and $\arg\{\mathrm{cor}(\boldsymbol{I}_{1,2}, e^{j(\boldsymbol{\theta}_{1,2})})\}$ [see (10)], one can conclude that the difference between the two angles and consequently $\Delta\varphi_{\mathrm{cov}}$ decrease by increasing homogeneity of $\boldsymbol{I}_{1,2}$. Fig. 1 features examples of interferometric phase histogram generated from semisynthetic interferograms. It illustrates intensity-dependent and intensity-independent phase contributions to the interferometric phase.

Fig. 2 illustrates histogram of closure phases generated from semisynthetic interferograms with the different statistical properties of intensity and phase changes. It can be seen that the shapes of interferogram histograms and closure phase histograms do not change by varying the magnitude of changes (compare the three histogram types of a, b, and c). This means that closure phase and interferometric coherence are independent of the magnitude of changes. Also, by comparing the histograms of Cluster 2 and Cluster 3, we can conclude that, when intensity and phase changes are independent (Cluster 2), the expected closure phase is zero. Unlikely, the expected closure phase becomes nonzero when intensity and phase changes are correlated (Cluster 3). These evaluations using synthetic data support our argument made in Section II [see (13)–(17)].

Next, we use real data to show that closure phase correlates with land cover types and is highly correlated with coherence values. We generated intensity-dependent [$\Delta\varphi_{\mathrm{cov}}$ in (9)] and intensity-independent [φ'_0 in (9)] phase images exploiting real SAR data. Using two images of ALOS-2 PALSAR-2 over Delta Junction (Alaska) taken on March 22, 2015 and March 6, 2016, we generated intensity-independent and intensity-dependent phases quantified in (9) and (10). Fig. 4 shows the study area. The three major land cover types on the images are scarcely to moderately vegetated soil (area I), forest (area II), and agricultural field (area III). The results are illustrated in Fig. 5. It can be seen that the intensity-independent phase [Fig. 5(a)] correlates with land cover type. This is because different land cover
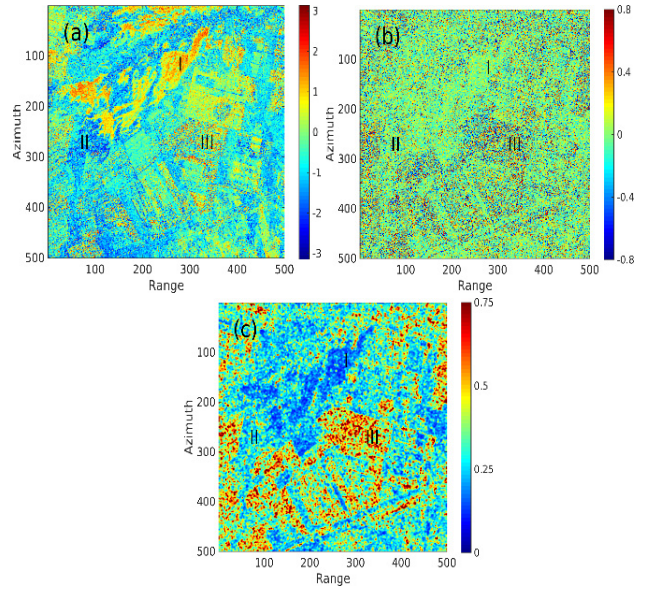

Fig. 5. (a) Intensity-independent phase [φ'_0 in (9)], (b) intensity-dependent phase [$\Delta\varphi_{\mathrm{cov}}$ in (9)], and (c) absolute intensity-dependent phase generated using ALOS-2 PALSAR_2 data over Delta Junction (Alaska).
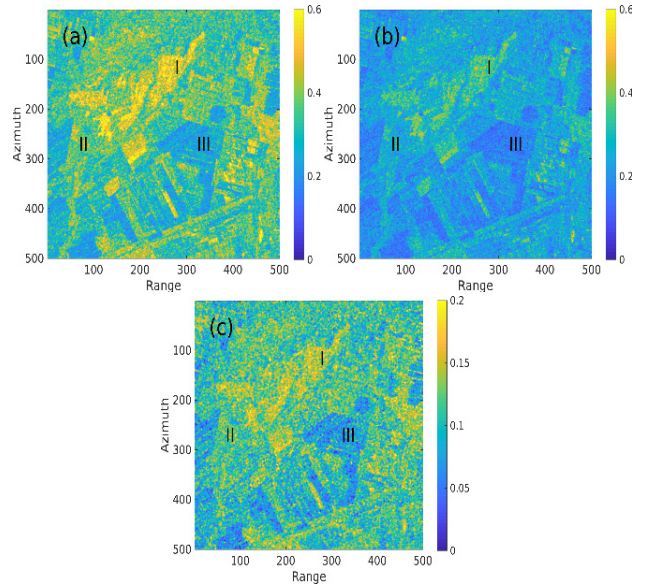

Fig. 6. (a) Interferometric coherence, (b) intensity-independent coherence [$|\hat{\gamma}_p|$ in (11)], and (c) difference between interferometric and intensity-independent coherences [intensity-dependent coherence [$\Delta|\hat{\gamma}_{\mathrm{cov}}|$ in (12)]]. The three major land cover types on the images are scarcely to moderately vegetated soil (area I), heavily vegetated area, forest (area II), and agricultural field (area III).

types experience different physical processes between the two images. Unlike intensity-independent phase [φ'_0 in (9)], the intensity-dependent phase [$\Delta\varphi_{\mathrm{cov}}$ in (9)] [Fig. 5(b)] is rather noisy. Its absolute value [Fig. 5(c)], however, correlates with land cover type to some extent. Small intensity-dependent phase values correspond to homogenous areas, where the coherence is higher and the larger values are associated with low-coherence areas (see Fig. 6 for comparison). This is because both coherence and $\mathrm{cov}(\boldsymbol{I}_{1,2}, e^{j(\boldsymbol{\theta}_{1,2})})$ increase by increasing the standard deviations of intensity and phase changes. Fig. 5 shows that the intensity-dependent phase does
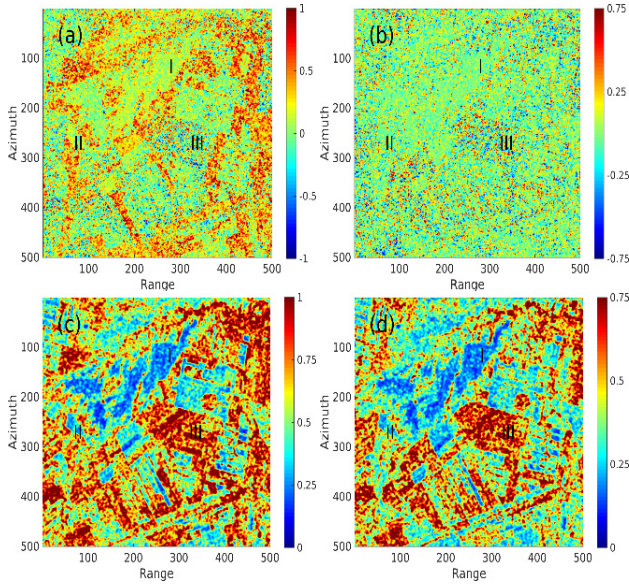
Fig. 7. (a) Closure phase of $\dddot{\varphi}_n$, (b) closure phase of $\Delta\dddot{\varphi}_{cov}$, (c) absolute closure phase of $\dddot{\varphi}_n$, and (d) absolute closure phase of $\Delta\dddot{\varphi}_{cov}$ generated using ALOS-2 PALSAR_2 data over Delta Junction (Alaska).

not possess information about physical changes but rather is a proxy to estimate the homogeneity of pixels.

In addition to phase contribution of the statistical properties of pixels, changes in multilooked coherence are also expected based on (12) and is shown in the phase histogram in Fig. 1. Fig. 6 shows the interferometric coherence (6a), intensity-independent coherence (6b), and intensity-dependent coherence [$\Delta|\hat{\gamma}_{\rm cov}|$ in (12)] (6c) that is the difference between the two coherence values. Also in Fig. 3, the length of vectors represent the magnitude of coherence values. The intensity-independent coherence (6b) is represented by the length of blue vector in Fig. 3. It is related to the phase statistics of single-looked pixels and independent of intensity statistics. The interferometric coherence (6a), on the other hand, is dependent on phase and intensity statistics. The intensity-dependent coherence [$\Delta|\hat{\gamma}_{\rm cov}|$ in (12)] is the length difference between green and blue vectors. In Fig. 3, it can be seen that the magnitude of interferometric coherence (the length of the green vector) increases by decreasing the difference between the phase of the statistical vector (red vector) and the phase of the intensity-independent vector (blue vector). The average intensity-dependent coherence of 0.1 can be seen on the image with lower amount on low-coherence pixels and higher values over homogenous areas.

Fig. 7 shows closure phase images generated using three images of ALOS-2 PALSAR-2 over Delta Junction (Alaska) taken on March 08, 2015, March 22, 2015, and March 6, 2016. As shown in (16), closure phase is a function of noise and statistical phases, $\dddot{\varphi}_n + \Delta\dddot{\varphi}_{\rm cov}$. Fig. 7(a) illustrates the phase triplet of $\dddot{\varphi}_n$ whereas, Fig. 7(b) illustrates the phase triplet of $\Delta\dddot{\varphi}_{\rm cov}$. $\dddot{\varphi}_n$ is a function of standard deviation of phase changes and its probability increases with a decrease in coherence. This means that high $\Delta\dddot{\varphi}_n$ values correlate with low coherence values as seen in Figs. 6 and 7(c). Fig. 7(d) shows that the absolute value of $\Delta\dddot{\varphi}_{\rm cov}$ is also correlated with

low coherence values. Therefore, we expect $\dddot{\varphi}_n$ and $\Delta\dddot{\varphi}_{\rm cov}$ to be correlated with each other and inversely with coherence, as in Figs. 6 and 7.

The mathematical analyses and the results of synthetic data show that none of the phase triplet components is directly related to the magnitude of phase or intensity changes. Rather, they are functions of the statistical properties. Also, our real data results show that absolute closure phase values correlate with coherence values. This fact makes the closure phase less appropriate for soil moisture change estimation.

B. Soil Moisture Estimation Using InSAR Phase and Closure Phase

As stated previously, in addition to deformation mapping, interferometric phase has been also used to estimate soil moisture changes [10], [11]. The change in soil moisture will induce a change in dielectric constant that in turn leads to phase increase, which is manifested as subsidence on interferograms [14], [15]. However, the phase of interferograms generated from single-looked pixels are rather noisy due to the strong effects of decorrelations and noises. Therefore, we prefer multilooked pixel. Multilooking reduces the noise and improves the reliability of phase unwrapping by averaging adjacent pixels in the complex interferogram [14], [15]. In practice, multilooking process makes strong pixels contribute more to interferometric phase. This is desired for deformation mapping purposes because the effect of weak pixels is canceled out to some extent. This leads to an increased effect of the strong pixels and lowers uncertainties in phase estimation.

For many cases, pixels are covered by natural materials, such as soil and vegetation layer. In these cases, the change in the physical properties of pixels, such as soil moisture and vegetation biomass changes, will cause intensity changes as well as phase changes. In this article, we showed that intensity changes can contribute to phase and coherence changes of multilooked pixels. The effect of the statistical properties of intensity on multilooked phase and coherence (10) are called intensity-dependent phase and coherence, respectively, in this article. The intensity-independent component of the multilooked interferometric phase is dominated by the change in the physical properties of the pixels plus a zero-mean random phase related to phase statistics within the multilooking window. The intensity-dependent phase is only associated with the statistical properties of the intensity and phase changes in the multilooking window. The intensity-dependent phase is rather small over homogeneous pixels but its magnitude increases over heterogeneous areas, such as pixels over vegetation layer. Therefore, understanding the contribution of intensity-dependent phase on InSAR phase, we suggest that care should be taken when multilooked phase is used to estimate absolute physical changes, especially over nonhomogeneous pixels.

Multilooking also leads to nonzero closure phase. It has been argued in the literature that closure phase has the potential to be used as a proxy to estimate soil moisture changes. We showed that closure phase is a function of phase and intensity statistical properties, and similar to InSAR coherence,

it contains no information about the magnitude of physical changes. It can be used for soil moisture estimation only when a strong correlation between absolute soil moisture changes and when its standard deviation can be found.

V. Conclusion

The magnitude and the standard deviation of phase changes associated with physical changes contribute to multilooked phase changes. InSAR coherence is related to the standard deviation of phase changes in the multilooking window. In this article, we showed that the statistical properties of the intensity of pixels contributes to phase and coherence of multilooked pixels. The influence of intensity increases by increasing the standard deviation of phase changes, dispersion index of intensity, and the correlation between intensity and phase changes. This article demonstrated that nonzero closure phase originates from the statistical properties of phase and intensity of the pixels within the multilooking window.

We showed that phase closure is associated with the standard deviation of phase changes and dispersion index of intensity, and does not relate to the magnitude of physical, deforming and nondeforming changes. Therefore, this casts doubt on the effectiveness of using phase triplet as a means to estimate soil moisture changes or any changes corresponding to dielectric changes.

Semisynthetic interferograms are used to support the findings of this article. Semisynthetic interferograms pair a real image and a synthetic SAR image, which are generated from the real SAR image by applying random changes in intensity and phase with defined magnitude of changes. We also used real SAR images to generate interferograms over different land cover types. The histogram of generated semisynthetic interferograms correspond well with the findings of the article.
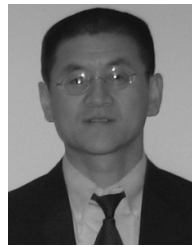
Acknowledgment

References

[1] D. Massonnet and K. L. Feigl, "Radar interferometry and its application to changes in the Earth's surface," *Rev. Geophys.*, vol. 36, no. 4, pp. 441–500, Nov. 1998.

[2] Z. Lu and D. Dzurisin, "InSAR imaging of Aleutian volcanoes: Monitoring a volcanic arc from space," *Geophysical Sciences*. Chichester, U.K.: Springer, 2014, p. 390.

[3] M. Shirzaei and R. Bürgmann, "Time-dependent model of creep on the Hayward fault from joint inversion of 18 years of InSAR and surface creep data," *J. Geophys. Res., Solid Earth*, vol. 118, no. 4, pp. 1733–1746, Apr. 2013.

[4] Y. Eshqi Molan, J.-W. Kim, Z. Lu, and P. Agram, "L-band temporal coherence assessment and modeling using amplitude and snow depth over interior alaska," *Remote Sens.*, vol. 10, no. 1, p. 150, 2018.

[5] A. Ferretti, C. Prati, and F. Rocca, "Permanent scatterers in SAR interferometry," *IEEE Trans. Geosci. Remote Sens.*, vol. 39, no. 1, pp. 8–20, Jan. 2001.

[6] Y. Eshqi Molan, J.-W. Kim, Z. Lu, B. Wylie, and Z. Zhu, "Modeling wildfire-induced permafrost deformation in an alaskan boreal forest using InSAR observations," *Remote Sens.*, vol. 10, no. 3, p. 405, 2018.

[7] R. P. Rykhus and Z. Lu, "InSAR detects possible thaw settlement in the alaskan arctic coastal plain," *Can. J. Remote Sens.*, vol. 34, no. 2, pp. 100–112, Jan. 2008.

[8] P. S. Agram *et al.*, "New radar interferometric time series analysis toolbox released," *Eos, Trans. Amer. Geophys. Union*, vol. 94, no. 7, pp. 69–70, Feb. 2013.

[9] H. Fattahi, F. Amelung, E. Chaussard, and S. Wdowinski, "Coseismic and postseismic deformation due to the 2007 M5.5 Ghazaband fault earthquake, Balochistan, Pakistan," *Geophys. Res. Lett.*, vol. 42, no. 9, pp. 3305–3312, 2015.

[10] F. De Zan, M. Zonno, and P. Lopez-Dekker, "Phase inconsistencies and multiple scattering in SAR interferometry," *IEEE Trans. Geosci. Remote Sens.*, vol. 53, no. 12, pp. 6608–6616, Dec. 2015.

[11] S. Zwieback *et al.*, "A statistical test of phase closure to detect influences on DInSAR deformation estimates besides displacements and decorrelation noise: Two case studies in high-latitude regions," *IEEE Trans. Geosci. Remote Sens.*, vol. 54, no. 9, pp. 5588–5601, Sep. 2016.

[12] Y. E. Molan and Z. Lu, "Modeling InSAR phase and SAR intensity changes induced by soil moisture," *IEEE Trans. Geosci. Remote Sens.*, early access, Feb. 17, 2020, doi: 10.1109/TGRS.2020.2970841.

[13] M. Nolan, D. R. Fatland, and L. Hinzman, "Dinsar measurement of soil moisture," *IEEE Trans. Geosci. Remote Sens.*, vol. 41, no. 12, pp. 2802–2813, Dec. 2003.

[14] S. Hensley *et al.*, "Effect of soil moisture on polarimetric-interferometric repeat pass observations by UAVSAR during 2010 canadian soil moisture campaign," in *Proc. IEEE Int. Geosci. Remote Sens. Symp.*, Jul. 2011, pp. 1063–1066.

[15] A. Ferretti, A. Fumagalli, F. Novali, C. Prati, F. Rocca, and A. Rucci, "A new algorithm for processing interferometric data-stacks: SqueeSAR," *IEEE Trans. Geosci. Remote Sens.*, vol. 49, no. 9, pp. 3460–3470, Sep. 2011, doi: 10.1109/TGRS.2011.2124465.

[16] R. M. Goldstein, H. A. Zebker, and C. L. Werner, "Satellite radar interferometry: Two-dimensional phase unwrapping," *Radio Sci.*, vol. 23, no. 4, pp. 713–720, Jul./Aug. 1988.

[17] G. Fornaro, S. Verde, D. Reale, and A. Pauciullo, "CAESAR: An approach based on covariance matrix decomposition to improve multibaseline–multitemporal interferometric SAR processing," *IEEE Trans. Geosci. Remote Sens.*, vol. 53, no. 4, pp. 2050–2065, Apr. 2015.

[18] S. Verde, D. Reale, A. Pauciullo, and G. Fornaro, "Improved small baseline processing by means of CAESAR eigen-interferograms decomposition," *ISPRS J. Photogramm. Remote Sens.*, vol. 139, pp. 1–13, May 2018.

[19] D. Just and R. Bamler, "Phase statistics of interferograms with applications to synthetic aperture radar," *Appl. Opt.*, vol. 33, no. 20, p. 4361, Jul. 1994, doi: 10.1364/AO.33.004361.

[20] Y. Anxi, W. Haijun, D. Zhen, and H. Haifeng, "Amplitude and phase statistics of multi-look SAR complex interferogram," *Defence Sci. J.*, vol. 64, no. 6, pp. 564–570, Nov. 2014.

[21] A. Lopes *et al.*, "Phase difference statistics related to sensor and forest parameters," in *Proc. Int. Geosci. Remote Sens. Symp. (IGARSS)*, Houston, TX, USA, 1992, pp. 779–781.

[22] R. Bamler and D. Just, "Phase statistics and decorrelation in SAR interferograms," in *Proc. IEEE Int. Geosci. Remote Sens. Symp.*, Aug. 1993, pp. 980–984.

[23] R. J. A. Tough, D. Blacknell, and S. Quegan, "Estimators and distributions in single and multi-look polarimetric and interferometric data," in *Proc. IEEE Int. Geosci. Remote Sens. Symp.*, vol. 4, Aug. 1994, pp. 2176–2178.

[24] J.-S. Lee, A. R. Miller, and K. W. Hoppel, "Statistics of phase difference and product magnitude of multi-look processed Gaussian signals," *Waves Random Media*, vol. 4, no. 3, pp. 307–319, Jul. 1994, doi: 10.1088/0959-7174/4/3/006.

[25] J.-S. Lee, K. W. Hoppel, S. A. Mango, and A. R. Miller, "Intensity and phase statistics of multilook polarimetric and interferometric SAR imagery," *IEEE Trans. Geosci. Remote Sens.*, vol. 32, no. 5, pp. 1017–1028, Sep. 1994, doi: 10.1109/36.312890.

[26] W. B. Davenport and W. L. Root, *An Introduction to the Theory of Random Signals and Noise*, 1st ed. New York, NY, USA: Institute Electr. Electron. Engineers, 1987, Ch. 8, pp. 158–165.

[27] R. Bamler and P. Hartl, "Synthetic aperture radar interferometry," *Inverse Problems*, vol. 14, no. 4, p. R1, 1998.

[28] R. J. A. Tough, D. Blacknell, and S. A. Quegan, "A statistical description of polarimetric and interferometric synthetic aperture radar data," *Proc. Roy. Soc. London. A, Math. Phys. Sci.*, vol. 449, no. 1937, pp. 567–589, 1995.

[29] P. Hoekstra and A. Delaney, "Dielectric properties of soils at UHF and microwave frequencies," *J. Geophys. Res.*, vol. 79, no. 11, pp. 1699–1708, Apr. 1974.

[30] M. T. Hallikainen, F. T. Ulaby, M. Dobson, M. A. El-Rayes, and L.-K. Wu, "Microwave dielectric behavior of wet soil—Part 1: Empirical models and experimental observations," *IEEE Trans. Geosci. Remote Sens.*, vol. GE-23, no. 1, pp. 25–34, Jan. 1985.

[31] C. J. Oliver and S. Quegan, *Understanding Synthetic Aperture Radar Images*. Norwood, MA, USA: Artech House, 1998.

Zhong Lu received the B.S. and M.S. degrees from Peking University, Beijing, China, in 1989 and 1992, respectively, and the Ph.D. degree from the University of Alaska Fairbanks, Fairbanks, Alaska, in 1996.

He was the Physical Scientist with United States Geological Survey, Vancouver, WA, USA, from 1997 to 2013. He is currently a Professor and Endowed Shuler–Foscue Chair with the Roy M. Huffington Department of Earth Sciences, Southern Methodist University, Dallas, TX, USA. He has published more than 200 peer-reviewed journal articles and book chapters focused on interferometric synthetic aperture radar (InSAR) techniques and applications, and a book on *InSAR Imaging of Aleutian Volcanoes: Monitoring a Volcanic Arc from Space* (Springer, 2014). His research interests include the technical developments of InSAR processing and their applications to the study of volcano, landslide, and human-induced geohazards.

Dr. Lu is a member of the NASA-India SAR (NISAR) Science Team since 2012, a Senior Associate Editor of journals *Remote Sensing* and *Frontier in Earth Sciences*, and a member of Editorial Boards of the *International Journal of Image and Data Fusion, and Geomatics, Natural Hazards and Risk*.

Yusuf Eshqi Molan received the B.S. degree from the Sahand University of Technology, Tabriz, Iran, in 2006, and the M.S. degree from the Amirkabir University of Technology, Tehran, Iran, in 2008. He is currently pursuing the Ph.D. degree in geophysics with Southern Methodist University, Dallas, TX, USA.
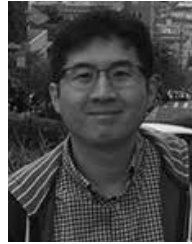
In 2008, he joined Remote Sensing Group, Geological Survey of Iran, Tehran. He was a Lecturer with the Sahand University of Technology, from 2010 to 2015. His research interests include the use of interferometric synthetic aperture radar (InSAR) for deformation mapping, and multi/hyper-spectral data processing and analysis. His main research focus is modeling the influence of soil moisture on InSAR measurements.

Jin-Woo Kim received the B.S. and M.S. degrees in civil engineering from Yonsei University, Seoul, South Korea, in 2005 and 2007, respectively, and the Ph.D. degree in geodetic science from The Ohio State University, Columbus, OH, USA, in 2013.

He is currently the Staff Scientist with the Roy M. Huffington Department of Earth Sciences, Southern Methodist University, Dallas, TX, USA, where he is investigating the earth surface processes with SAR imagery and Interferometric synthetic aperture radar (InSAR) methods. His research interests include InSAR applications to understand wetland hydrology, sinkhole evolution, landslide mechanisms, and interactions between human activities and surface/underground processes.